Front. Struct. Civ. Eng.
https://doi.org/10.1007/s11709-020-0674-8

RESEARCH ARTICLE

# Effect of a less permeable stronger soil layer on the stability of non-homogeneous unsaturated slopes

**Nabarun DEY*, Aniruddha SENGUPTA**

*Department of Civil Engineering, Indian Institute of Technology Kharagpur, Kharagpur 721302, India*
**Corresponding author. E-mails: nabarun@iitkgp.ac.in; nabarundey88@gmail.com*



**ABSTRACT** Slope failure occurs due to an increase in the saturation level and a subsequent decrease in matric suction in unsaturated soil. This paper presents the results of a series of centrifuge experiments and numerical analyses on a 55° inclined unsaturated sandy slope with less permeable, stronger silty sand layer inclusion within it. It is observed that a less permeable, stronger silty sand layer in an otherwise homogeneous sandy soil slope hinders the infiltration of water. The water content of the slope just above the stronger layer increases significantly, compared to elsewhere. No shear band is found to initiate in a homogeneous sandy soil slope, whereas for a non-homogeneous slope, they initiate just above the less pervious, stronger layer. A discontinuity of the shear zone is also observed for the case of a non-homogeneous soil slope. The factor of safety of a non-homogeneous, unsaturated soil slope decreases because of the less permeable, stronger layer. It decreases significantly if this less permeable, stronger soil layer is located near the toe of the slope.

**KEYWORDS** non-homogeneous slope, stronger soil layer, factor of safety, centrifuge model test, unsaturated soils

## 1 Introduction

Sliding failures of natural slopes, roadway and railway embankments, and industrial dump fills are abundant. Depending on the location of the failed slope, a sliding failure can cause a serious disaster in terms of loss of life and property damage [1,2]. Rainfall-triggered slope failures are common in India, China, and Latin America [3–5]. Rainwater infiltrates earthen slopes and increases the pore water pressure and the degree of saturation [6,7]. Increasing saturation and the consequent decrease in the matric suction pressure of soil are reasons behind the reduction in the shear strength of unsaturated soil [8–11]. This decrease in the effective stress [12] within the soil slope eventually leads to slope failure.

Naturally occurring soil slopes are seldom homogeneous. They may consist of layers of different types of soil [13,14]. Some of the layers may be weaker or stronger than the overall soil mass, resulting in a complicated stability mechanism. The behavior of unsaturated soil slopes with non-homogeneous layers has been investigated using different methods, such as model tests, field studies, and numerical analyses [15]. Most of the relevant research works are focused on the failure mechanism of non-homogeneous soil slopes with embedded weak layers [16,17]. Al-Homoud and Tubeileh [18] studied three different cut slopes in Jordan and concluded that the majority of the cut slope failures occurred because of the presence of weak soil layers consisting of marl, clay, or shale within the soil slopes. Wang et al. [19] have reported the results of a series of centrifuge tests on slopes with weak montmorillonite layers under rainfall conditions and concluded that the weak layers accelerate slope failure by increasing the rate of infiltration and excess deformations. The study of the stability mechanism for non-homogeneous unsaturated soil slopes due to the presence of stronger but less permeable soil layers has not received enough attention. The common belief among engineers is that the presence of a stronger layer within an otherwise homogeneous soil slope is of no concern, because the stronger soil layer will not fail or will fail later. However, if the relatively stronger soil layer has less permeability, it will hinder the natural flow of the infiltrated rainwater or groundwater, resulting in pore water pressure buildup within the slope. With the buildup of pore water pressure within the soil slope, the effective stresses within the soil

*Article history: Received Sep 17, 2019; Accepted Nov 8, 2019*

are reduced, which can trigger a slope failure. The present study intends to explore the effect of less permeable, stronger soil layer intrusion on the stability mechanism of unsaturated, non-homogeneous soil slopes by conducting centrifuge model tests, as well as by implementing finite element analysis using GeoStudio-2007 [20]. The small-scale laboratory model tests do not often replicate actual slope behaviors observed in the field, because geo-materials exhibit scale effects. In addition, there are difficulties in comparing the results between the prototype and the small-scale laboratory model, because a difference in stress levels exists between them. Some of these problems related to the scaling effects of small-scale model tests can be overcome in centrifuge model tests. In a centrifuge model test, a stress level similar to that of the prototype is achieved by increasing the g-level during the model tests. The results of centrifuge tests on non-homogeneous, unsaturated sandy slopes are compared with the results of the corresponding numerical analyses to gain confidence and insight into the failure mechanisms in such cases.

## 2 Description of centrifuge model tests

The laboratory model tests were conducted on a beam-type centrifuge available at Universität für Bodenkultur (BOKU), Vienna, Austria. It essentially consists of a steel beam balanced at the middle and rotated at a very high speed by a motor. The motor can apply a maximum acceleration of 200*g* at 400 r/min. The length of the steel beam is 2.6 m. The steel beam has two baskets (basket-A and basket-B) hanging at each end (refer to Fig. 1). During the test, a test box, with the small-scale model in it, was fixed to the base of basket-A. An equivalent amount of weight was placed in basket-B to balance the steel beam. In addition, one fixed balance was utilized. The fixed balance was rotated to ensure that the rotating beam was balanced perfectly and that both arms floated symmetrically. Next, the whole system was rotated at a predetermined speed to apply a predetermined g-force to the small-scale model, and the required measurements were made.

In the present study, all the tests are conducted in a 480 mm ($L$)×155 mm ($B$)×450 mm ($H$) aluminum box (refer to Fig. 2(a)). For monitoring and image capturing during the centrifuge test, one side of the test box was made of acrylic glass. The weight of the empty box was 40 kg. In addition, the test box was waterproof. To minimize the friction between the walls of the test chamber and the soil model placed inside the box, silicon oil was sprayed uniformly on the inside walls of the box. To obtain good quality pictures during the centrifuge test, a high-speed camera and two lighting systems are installed within the centrifuge basket (see Fig. 2(b)).

One homogeneous soil slope and two non-homogeneous soil slopes with a less pervious, stronger soil layer located at different heights of the slope were prepared for the laboratory centrifuge tests. The homogeneous soil slope was constructed with poorly graded sand at a relative density of 60%. The non-homogeneous soil slopes were also made of the same poorly graded sand, but with a 25-mm-thick stronger, less permeable layer of silty sand in the middle or at the base of the slope. The stronger silty sand layer was also compacted at an identical density. The test results of the homogeneous soil slope were utilized to determine the significance of the presence of the stronger, less-permeable soil layer within the otherwise homogeneous soil slope.

Before the construction of the model slopes for the centrifuge tests, 10% water was added to the oven-dried sand and was thoroughly mixed. Initially, a 50-mm-thick horizontal sand base with a relative density of 60% was prepared by compacting a predetermined quantity of sand using a Proctor hammer. A 200-mm high model soil slope was then constructed over the horizontal base in eight horizontal lifts, each 25-mm thick. Each lift was constructed by compacting a pre-calculated quantity of sand with a Proctor hammer to achieve a relative density of 60%. In the present study, for eight soil layers, eight airtight containers were used to mix water with soil, and were used one by one, so that there would not be any loss of moisture content. For the non-homogeneous slope with the stronger soil layer, the oven-dried silty sand with a 10% water content was placed in the same way at the bottom or in the middle of the 200-mm-high slope and was compacted with a Proctor hammer to achieve a compacted height of 25-mm. To prepare the required slope after compaction, the walls of the model box were opened very carefully and immediately replaced by two supporting plates. Both supporting plates had already been shaped at a 55° inclined slope. Figure 3 shows the detailed procedure for constructing the laboratory model slope. Before cutting the slope, penetration tests were conducted to verify the uniformity and quality of the prepared soil slopes. Subsequently, a 55° slope was constructed by cutting and shaping the compacted horizontal soil layers in two steps. In the first step, the soil was removed with a shovel by maintaining some distance from the actual slope surface, and the layer-wise moisture content was measured. In the second step, the final slope was constructed by cutting the remaining soil using a very sharp spatula so that the soil remained undisturbed. After making a perfectly fine shape of the 55° slope, both supporting plates were quickly replaced by the model box walls, and the top plate was placed immediately to prevent moisture loss. Figure 4 shows the geometry of the 55° inclined homogeneous and non-homogeneous model slopes.

After the preparation of the slopes, the air-tight test box with the soil slope in it is mounted on basket-A of the beam centrifuge (see Fig. 1), the centrifuge is accelerated slowly from 1*g* to 40*g*, and the required data were recorded digitally at 10-s intervals. After the centrifuge tests, soil

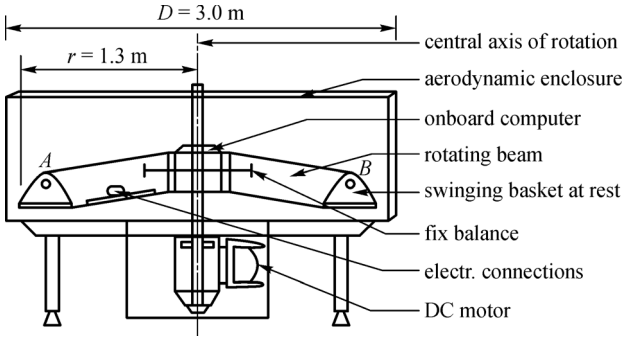


**Fig. 1** Schematic diagram of the centrifuge used at BOKU.

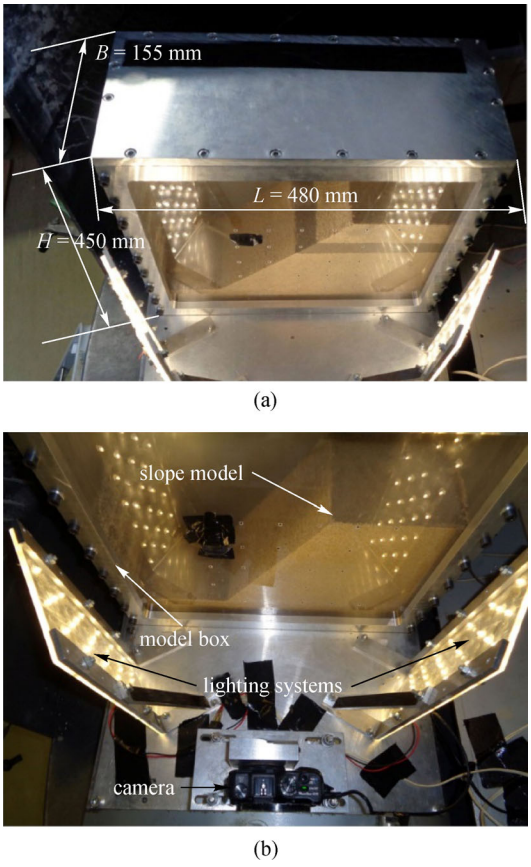


**Fig. 2** (a) Centrifuge test box with (b) camera and lighting arrangements.

samples were collected along the slopes from top to bottom at intervals of 25-mm to determine the moisture content. In addition, for the case of non-homogeneous slopes, the soil samples were collected from just above, from the middle, and just below the non-homogeneous layer. For numerical analysis, the moisture content was obtained in the middle of the same sampling locations. The centrifuge test has the advantage of simulating the same stress level as that of the prototype in a small-scale model by increasing the *g*-force (centrifugal force) during the test. The centrifugal force has a direct impact on the scaling factor ($N$) [21], which can be represented as

$$N = \frac{\omega^2}{g} r, \tag{1}$$

where $\omega$ is the angular velocity; $g$ is the acceleration due to gravity; and $r$ is the distance from the centrifuge axis. Table 1 summarizes the model and prototype dimensions, as well as the properties of the slopes and its materials according to the scaling law in a centrifuge model test given by Taylor [22] and Ng et al. [23]. In this study, a scaling factor of 40 was assumed for all the reported centrifuge tests. This gives a prototype slope height of 8-m, which is a typical value for the road and the railway side slopes in this part of the world [24,25]. Images of the slopes, taken by an onboard camera during the experiments, were processed using Geo-PIV software [26]. To analyze the deformations of the slopes and the formation of shear bands, digital images of the slope at 5*g* intervals were selected. For the case of slope failure occurring in the centrifuge, the last image just before the failure was considered for the image analysis. From the image analysis, the deformation vectors were plotted, and the strains within the soil slopes were obtained.

## 3 Material properties of soils

The poorly graded sand utilized in the preparation of the homogeneous and non-homogeneous soil slopes has an internal friction angle of 34° and a cohesion of 0.4 kN/m$^2$. All the slopes have an initial moisture content of 10% and a dry density of 1.54 g/mL, which yields a relative density of 60% for the soil. The silty sand utilized in the preparation of the less permeable, stronger soil layer within the otherwise homogeneous sandy slope has an angle of internal friction of 32.5° and a cohesion of 5.4 kN/m$^2$. This layer is also prepared at an initial moisture content of 10% and at the same density to maintain consistency between the soil slopes tested. The unsaturated permeability of the silty sand ($4.8\times10^{-6}$ m/s) is much less than the unsaturated permeability of poorly graded sand ($1.1\times10^{-4}$ m/s). Table 2 shows the material properties of the sand and silty sand. The grainsize distribution curve is shown in Fig. 5.

## 4 Numerical modeling

Numerical analysis is performed on the prototype scale. In this study, the height of the prototype slopes is 8-m. Table 1 summarizes the model and prototype dimensions. The two-dimensional slopes considered in this study (i.e., a homogeneous sandy slope; and a sandy slope with a less pervious, stronger silty sand layer at the bottom, and at the

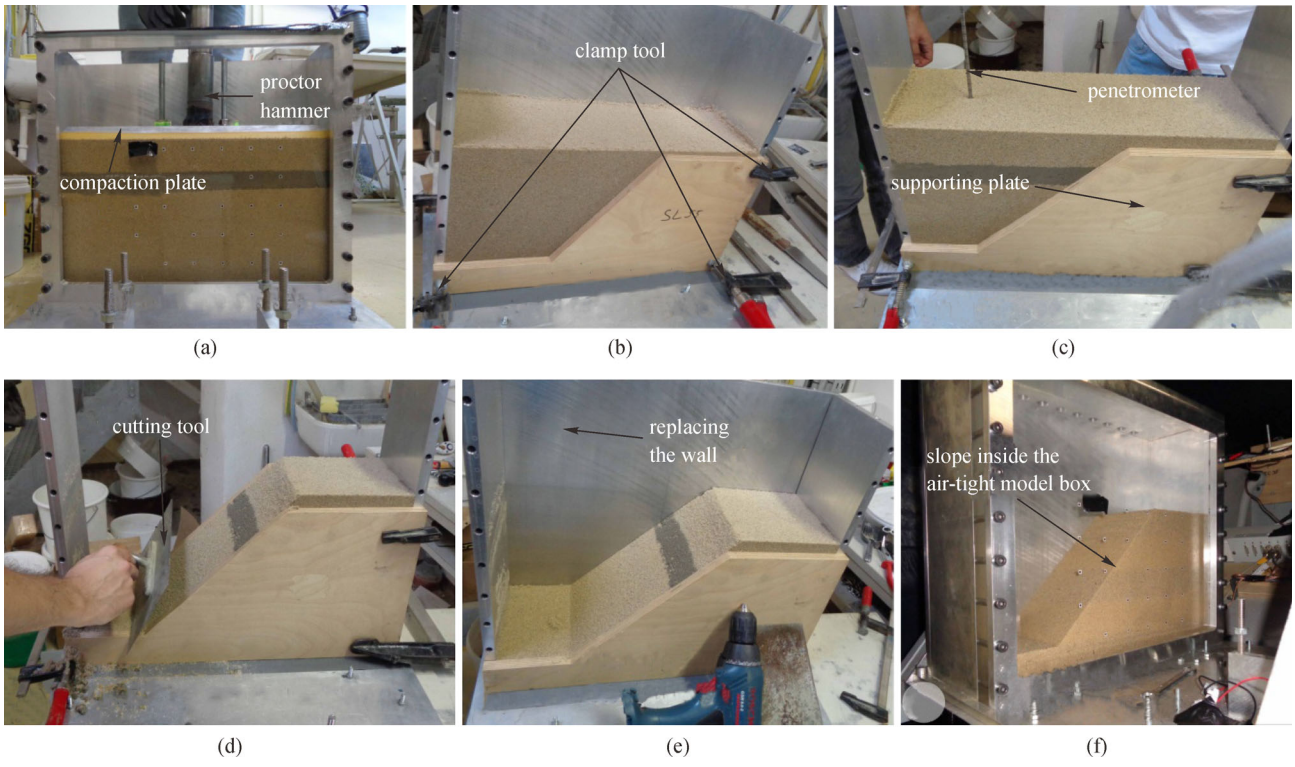


**Fig. 3** Procedure for constructing the laboratory model slope. (a) Soil compaction; (b) attaching supporting plate; (c) penetration test; (d) cutting and shaping; (e) attaching model box; (f) required model slope.

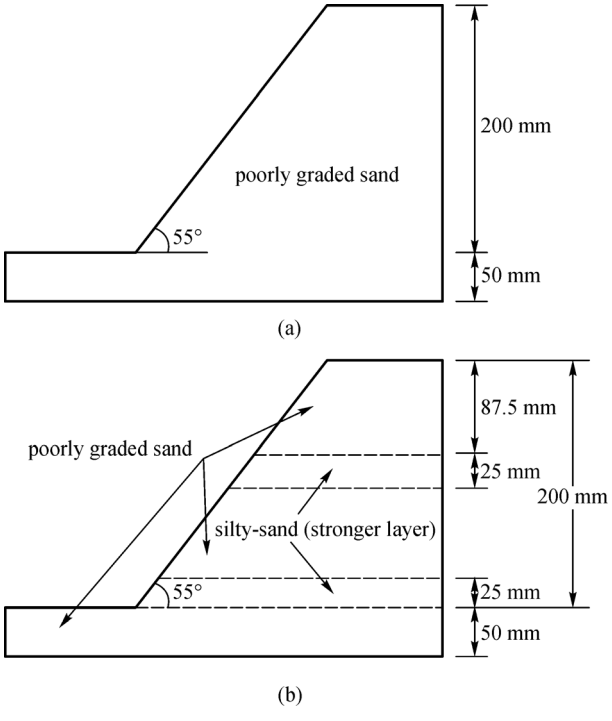


**Fig. 4** Geometry of the slopes. (a) Homogeneous; (b) non-homogeneous.

mid-height of the slope) are numerically discretized by three-node triangular elements and four-node quadrilateral elements. It is assumed that the two vertical side boundaries of the model are fixed in the $x$-direction, while the bottom boundary is considered to be fixed in both the $x$- and $y$-directions. Figure 6 shows the discretized geometry for the case of the non-homogeneous slope with a stronger layer at the mid-height.

The stability of the slope is calculated by considering the slope geometry and the shear strength with respect to the hydrostatic condition. Matric suction is an important stress variable that has a direct influence on the shear strength of the unsaturated soil [8,10]. The suction stress ($\sigma_s$) is a characteristic function of suction pressure and soil saturation [27], which can be obtained through the following closed-form equation:

$$\sigma_s = f(u_a - u_w), \tag{2}$$

where $u_a$ is the pore air pressure; $u_w$ is the pore water pressure; and $(u_a - u_w)$ is the matric suction.

The hydrostatic behavior of the unsaturated slopes is investigated using the SEEP/W module of GeoStudio. The SEEP/W module was developed based on the theory of fluid flow through porous media, in which the water flow within the saturated media, along with the unsaturated media, strictly obeys Darcy's law [28,29], and can be expressed by the following equations:

$$q = kiA, \tag{3a}$$

**Table 1** Scaling factors for centrifuge tests

| parameters | scaling factor (model/prototype) | unit | model dimension | prototype dimension |
|---|---|---|---|---|
| basic parameters | | | | |
| length of slope | $1/n$ | mm | 480 | 19200 |
| width of slope | $1/n$ | mm | 155 | 6200 |
| height of slope | $1/n$ | mm | 250 | 10000 |
| density of soil | 1 | g/mL | 1.54 | 1.54 |
| hydraulic parameters | | | | |
| permeability of sand ($k1$) | $n$ | m/s | $1.1\times10^{-4}$ | $2.75\times10^{-6}$ |
| permeability of silty sand ($k2$) | $n$ | m/s | $4.8\times10^{-6}$ | $1.2\times10^{-7}$ |
| hydraulic gradient ($i$) | 1 | – | – | – |
| suction | 1 | $N/m^2$ | – | – |

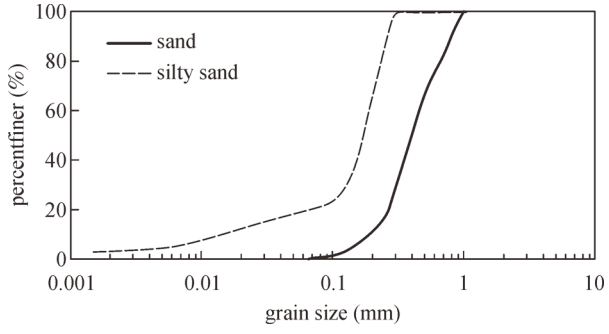


**Fig. 5** Grain size distribution curves for the sand and silty sand.

$$v = ki, \tag{3b}$$

where $q$ is the specific discharge; $v$ is the Darcian velocity of flow; $k$ is the coefficient of permeability; $i$ is the gradient of the hydraulic head; and $A$ is the cross-sectional area of the soil.

The sand and silty sand slope materials are modeled by a saturated/unsaturated material model, where the unsaturated hydraulic conductivity and the volumetric water content are defined by the van Genuchten [30] relationship. Figures 7(a) and 7(b) show the relationship between the volumetric water content vs. matric suction, and the degree of saturation vs. matric suction, respectively, for both soils utilized in this study. Equation (4a), proposed by van Genuchten [30], gives the relationship between the hydraulic conductivity ($k_w$) at a given suction pressure ($\psi$) and the hydraulic conductivity of the saturated soil ($k_s$):

$$k_w = k_s \cdot \frac{[1-(a\psi^{(n-1)})(1+(a\psi^n))^{-m}]^2}{\left[\{(1+a\psi)^n\}^{\frac{m}{2}}\right]}, \tag{4a}$$

where $a$, $n$, and $m$ are the curve-fitting parameters. The corresponding relationship between the volumetric water content ($\Theta_w$) at a given suction pressure, and the saturated ($\Theta_s$) and residual ($\Theta_r$) volumetric water content is expressed as follows:

**Table 2** Material properties of sand and silty sand

| properties | unit | sand | silty sand |
|---|---|---|---|
| percentage of coarse, medium and fine sand | % | 0, 69.5, 30.4 | 0, 0.1, 90.1 |
| percentage of gravel and fines content | % | 0, 0.1 | 0, 9.8 |
| $D_{10}$, $D_{30}$, $D_{60}$ | mm | 0.19, 0.3, 0.47 | 0.08, 0.14, 0.2 |
| uniformity coefficient, $C_u$ | – | 2.47 | 2.5 |
| coefficient of curvature, $C_c$ | – | 1.01 | 1.23 |
| specific gravity, $G$ | – | 2.62 | 2.71 |
| maximum dry unit weight | $kN/m^3$ | 16.3 | 16.78 |
| minimum dry unit weight | $kN/m^3$ | 13.9 | 12.95 |
| maximum void ratio, $e_{max}$ | – | 0.86 | 1.05 |
| minimum void ratio, $e_{min}$ | – | 0.58 | 0.58 |
| permeability, $k$ | m/s | $1.1\times10^{-4}$ | $4.8\times10^{-6}$ |
| cohesion, $C$ | $kN/m^2$ | 0.4 | 5.4 |
| angle of internal friction, $\varphi$ | degree | 34 | 32.5 |

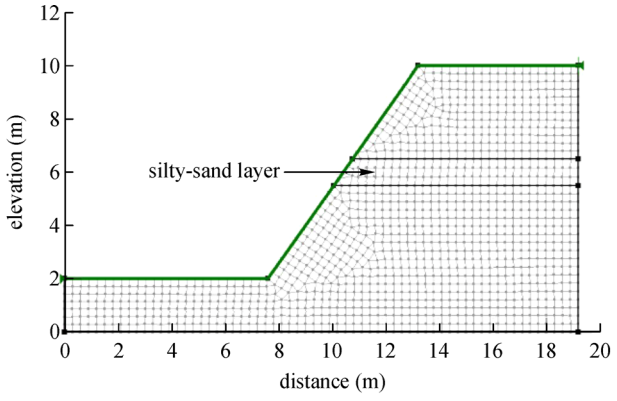


**Fig. 6** Discretized slope (with one stronger soil layer at mid-height).

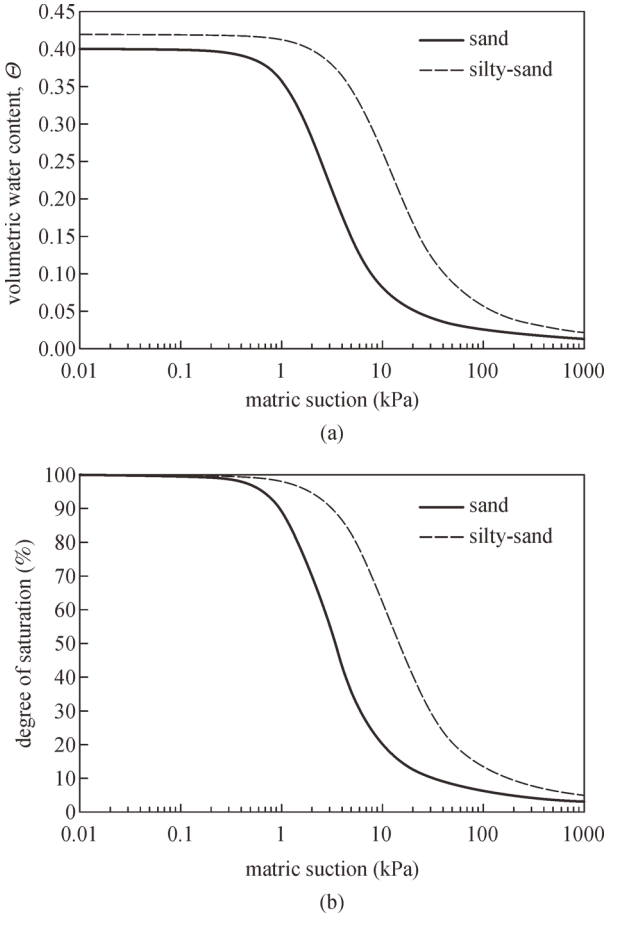


**Fig. 7** Variation of (a) volumetric water content with suction pressure; (b) degree of saturation with matric suction.

$$\Theta_{\mathrm{w}} = \Theta_{\mathrm{r}} + \frac{\Theta_{\mathrm{s}} - \Theta_{\mathrm{r}}}{\left(1 + \left(\frac{\psi}{a}\right)^{n}\right)^{m}}. \tag{4b}$$

Fredlund and Xing [31] proposed an alternative to Eq. (4b), which can be utilized to expand the volumetric water content ($\Theta_{\mathrm{w}}$) function for a wide range of soil suction, up to $10^6$ kPa:

$$\Theta_{\mathrm{w}} = C_{\psi} \frac{\Theta_{\mathrm{s}}}{\left(\ln\left[\mathrm{e} + \left(\frac{\psi}{a}\right)^{n}\right]\right)^{m}}, \tag{5}$$

where $C_{\psi}$ is a correction function.

It is assumed that the soil slopes are in an unsaturated condition at the beginning of the tests, with the initial water content at 10%, as in the laboratory centrifuge tests, and the no-flow boundary condition is applied at the bottom-most level of the model slopes. The reason behind the assumption of the no-flow boundary at the very bottom of the model is that the centrifuge test box is completely waterproof in the present study; thus, during the centrifuge operation, seepage water flows in a downward direction and no water can flow outside the box. As a result, water starts accumulating at the bottom of the slope model. Similarly, in the numerical analysis, a no-flow boundary is considered at the bottom of the slope model, so that if seepage water reaches this point, then the water should accumulate. Considering these initial conditions, the initial pore water pressure and the suction profile within the slopes are developed using the SEEP/W program.

The slope geometry and the results obtained from the steady-state seepage analysis were exported to the SLOPE/W module of GeoStudio for stability analysis of the slopes. The SLOPE/W module is designed based on the principle of limit equilibrium of forces and moments to calculate the factor of safety (*FOS*). The limit equilibrium method implies that the *FOS* of the frictional part of the strength and the cohesive part of the strength remains consistent for the whole soil grains, and the *FOS* is also constant at every point of the failure plane. The program calculates the *FOS* against sliding using the simplified Bishop's method [32], the ordinary method of slice, and Janbu's method [33] for slope stability analysis. These methods are distinct because of the assumptions made for the interslice forces fulfilling the moment equilibrium or force-equilibrium. The simplified Bishop's method of limit equilibrium slope stability analysis only satisfies the moment equilibrium condition by assuming that the interslice forces are horizontal. The ordinary method of slice of limit equilibrium only satisfies the moment equilibrium and ignores the interslice forces. Janbu's method of limit equilibrium slope stability analysis only satisfies the force equilibrium by assuming that the interslice forces are horizontal. This is done only to check and compare the variations in the *FOS* and the position of the slip circle for each case. However, only the positions of the critical slip circles and the corresponding critical *FOS* computed by the simplified Bishop's method are reported.

In unsaturated soil mechanics, the matric suction pressure has a direct influence on the shear strength [8], which can be expressed as

$$S = C' + (\sigma_{\mathrm{n}} - u_{\mathrm{a}})\tan\phi' + (u_{\mathrm{a}} - u_{\mathrm{w}})\tan\phi^{\mathrm{b}}, \tag{6}$$

where $S$ is the shear strength; $C'$ is the effective cohesion; $\sigma_n$ is the total normal stress; $\phi'$ is the effective friction angle; and $\phi^b$ is an angle defining the increase in the shear strength for an increase in the suction. Vanapalli et al. [10] introduced the concept of volumetric water content to determine the shear strength of unsaturated soil, and the modified equation can be written as

$$S = C' + (\sigma_n - u_a)\tan\phi' + (u_a - u_w)\left[\left(\frac{\Theta_w - \Theta_r}{\Theta_s - \Theta_r}\right)\tan\phi'\right]. \quad (7)$$

A plane strain condition was assumed in the slope stability analysis. The primary geometry of the slopes, including the hydrostatic statuses, is imported from the seepage analysis. In the stability analysis, the modified Mohr-Coulomb constitutive model for unsaturated soil is utilized to model the engineering behavior of the soils. The geotechnical properties of the soils, as obtained from the laboratory tests, are listed in Table 1. The inherent sliding portion is discretized into several vertical slices. Normal stress and shear stress are determined for each vertical slice at the slice base. Figure 8 shows all the forces acting on slice number 14 from the bottom. The shear strength of each slice is then calculated with the normal stress along with the shear parameters and matric suction. The computed stresses are then converted into forces by simply multiplying the stress values by the length of the slice. Once the resisting shear forces and the driving shear forces are obtained for each of the slices, the *FOS* is computed by integrating the forces over the length of the possible failure plane. Equations (8) and (9) are used to determine the *FOS* of the potential failure plane corresponding to the force and moment equilibrium methods, respectively.

$$FOS = \frac{\sum s_r}{\sum s_m}, \quad (8)$$

where $\sum s_r$ is the total resisting shear force; and $\sum s_m$ is the total driving shear force along the failure plane.

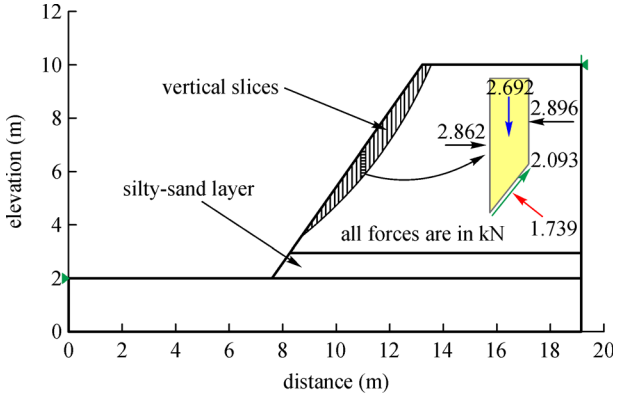


**Fig. 8** A potential sliding zone with vertical slices for the case of a non-homogeneous layer at the base of the slope.

$$FOS = \frac{\sum(S_r l_{base})I}{\sum(S_m l_{base})I}, \quad (9)$$

where $l_{base}$ is the base length of the vertical slice; and $I$ is the slice index.

A grid search technique was employed to obtain the most critical failure plane with the minimum *FOS* for each case. In this procedure, a significant number of circular failure planes are created for each case with different centers of the circle, different radii of the slip circle, and different bottom-most elevations of the slip circle. The *FOS* is computed for all possible slip surfaces, and the one with the lowest *FOS* is selected as the most critical for the given condition.

## 5 Interpretation of experimental and numerical results

### 5.1 Variations of water content

The water content of the slope materials plays an important role in the stability of the soil slope. A high water content of the soil reduces the suction pressure and consequently lowers the stability of the slope. On the other hand, a lower water content of the soil increases the suction pressure and, consequently, the stability of the soil slope increases. The measured and computed variations of the water content with respect to the depth of the slopes are depicted in Fig. 9 for the three cases. The solid lines represent the results of the numerical analysis, while the dashed lines represent the observed experimental results. During the centrifuge operation, the $g$-force increases and the deformation process initiates, with the water within the slope moving in the downward direction. The overall water content variations with respect to the depth of the slope are almost the same for all the cases, other than the surrounding areas of the non-homogeneous layer. During the tests, it was observed that the water content of the soil decreased in the upper portion of the slope, compared with the lower portion. However, before the tests, the water content of the entire slope was almost uniform. For the case of non-homogeneous slopes, the water content in the relatively stronger and impermeable silty sand layer and just above it was much higher than those at other depths. The stronger layer has less permeability and prevents the water from moving freely in the downward direction; consequently, the water content just above the stronger layer increases. This weakens the slope, because the effective strength of the soil decreases with an increasing degree of saturation of the soil layer.

Figure 10 shows the critical slip surfaces and the corresponding *FOS* obtained from the numerical analysis. For the case of a homogeneous slope (see Fig. 10(a)), a critical slip surface corresponding to a minimum *FOS* of 1.3 is found just above the toe of the slope. The value of the

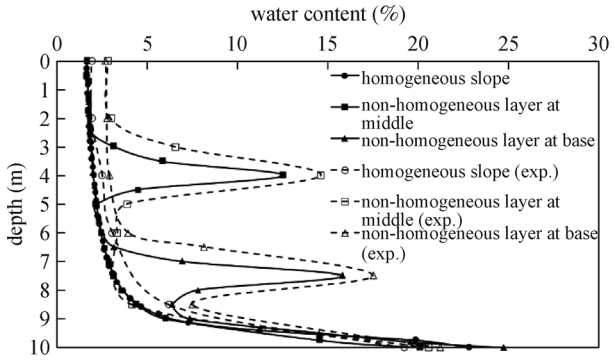


**Fig. 9** Water content variation of the slopes (in prototype scale).

safety factor is adequate, and no stability issues were noticed, even in the model tests. For the case of a slope with a stronger layer at the mid-slope height (see Fig. 10(b)), a critical slip surface corresponding to a minimum *FOS* of 1.09 is found from the numerical analysis. The slip surfaces develop just above the non-homogeneous stronger layer. Because the value of the safety factor is slightly greater than one, no instability is observed or predicted for this case. For the case of a slope with a stronger layer at the base (see Fig. 10(c)), a critical slip surface with an *FOS* of less than one (0.91) is determined from the numerical analysis. The slope for this case is found to fail at 40*g* in the centrifuge tests, while the other two slopes (homogeneous slope and non-homogeneous slope with the stronger layer at mid-height) remain stable. Thus, the less permeable, stronger layer significantly affects the stability of the slope due to the changes in the infiltration process. The value of the *FOS* also decreases with an increasing depth of the less permeable, stronger soil layer.

### 5.2 Deformations of the slopes

The deformations of the slopes during the model tests were analyzed using Geo-PIV, which essentially plots the slope deformations in vector form. Figure 11 shows the deformation vectors for all three cases at the end of the tests. The presence of a less permeable, stronger silty sand layer was found to significantly affect the deformation of the slopes. It was observed that there are significant deformations of the soil slopes before the failure because of settlement. Thereafter, rotational movements were noticed at failure. It was also observed that for the case of the non-homogeneous slopes, there was almost no soil deformation below the stronger silty sand layer, and the outward failure movement initiates from just above the stronger layer (Figs. 11(b) and 11(c)). For the case of the homogeneous slope, no significant deformation (rotational) of the soil slope is observed (Fig. 11(a)). A notable difference in soil deformation was observed just above the non-homogeneous soil layer, which indicates that there is a

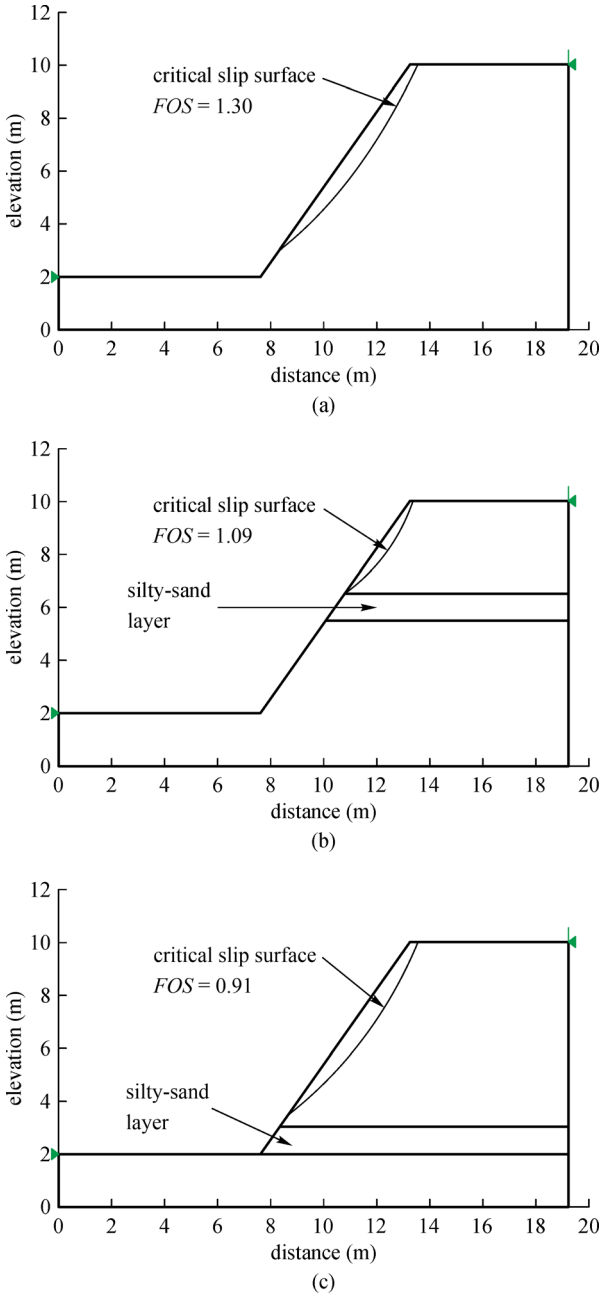


**Fig. 10** Critical slip surfaces and the corresponding *FOS*. (a) Homogeneous slope; (b) non-homogeneous layer in the middle; (c) non-homogeneous soil layer at the base of the slope.

significant influence from the presence of a stronger and less permeable silty sand layer on the slope deformation. The silty sand layer prevents water from easily infiltrating and, consequently, the water content above this layer increases, which reduces the strength and increases the deformation in the soil just above it.

### 5.3 Failure mechanism and localization of strains

The progressive nature of the development of the shear

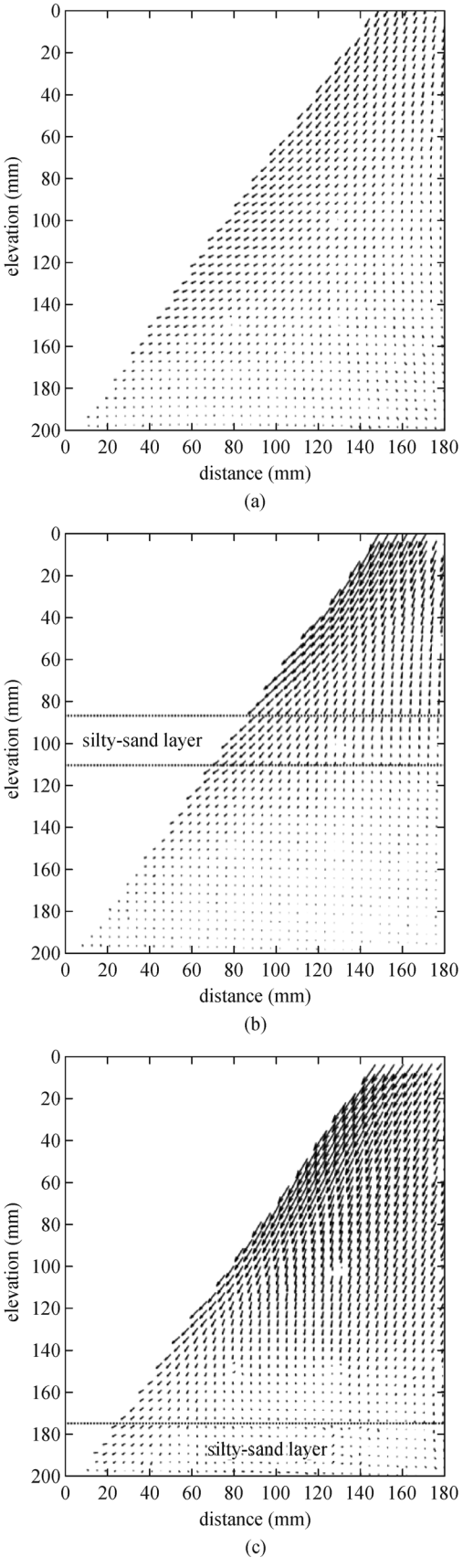


**Fig. 11** Deformation vectors within the slopes after centrifuge tests. (a) Homogeneous slope; (b) non-homogeneous layer at mid-height; (c) non-homogeneous layer at base.

band can be observed using Geo-PIV and the numerical studies (GeoStudio-2007). Figures 12–15 show the shear strain contour plot, which is obtained from the experimental analysis (Geo-PIV).

For the case of a homogeneous slope, it is observed that there is no significant shear strain until 35*g* (see Fig. 12(a)). At 40*g* (see Fig. 12(b)), a shear zone develops. However, because of the small deformations, no shear band is observed from the image analysis, which could lead to the collapse of the slope. In the numerical analysis, a critical slip surface corresponding to a minimum *FOS* of 1.30 is found just above the toe of the slope (refer to Fig. 10(a)). Because the value of the safety factor is adequate, no stability issues are predicted.

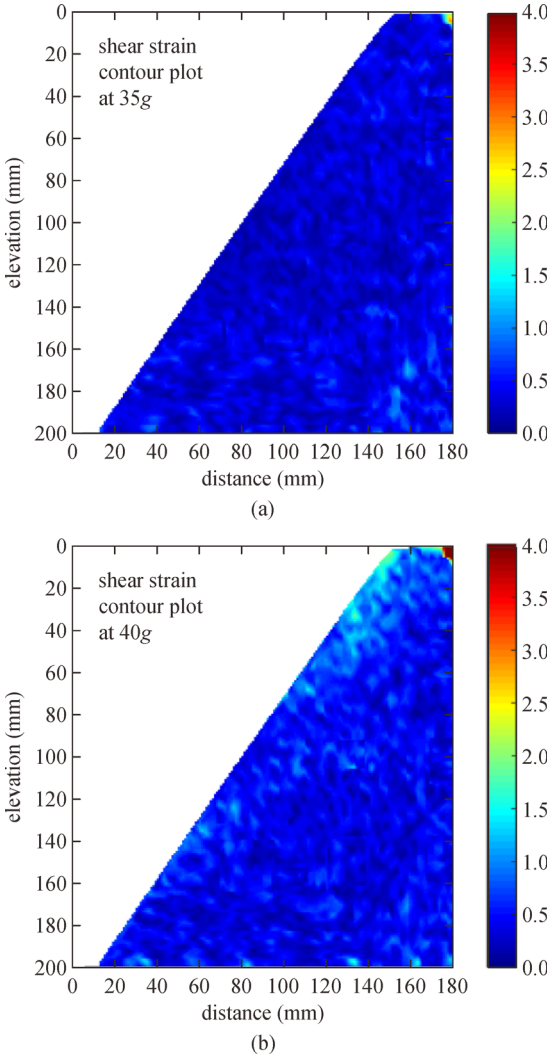


**Fig. 12** Formation of shear strain fields in the homogeneous slope during (a) 35*g*; (b) 40*g*.

Figure 13 shows the progressive nature of the shear strain fields for the case of a non-homogeneous slope with a stronger silty sand layer at the mid-slope height. No significant shear strains are observed until 20*g*. From 30*g* onward, a significant number of shear strains are observed,

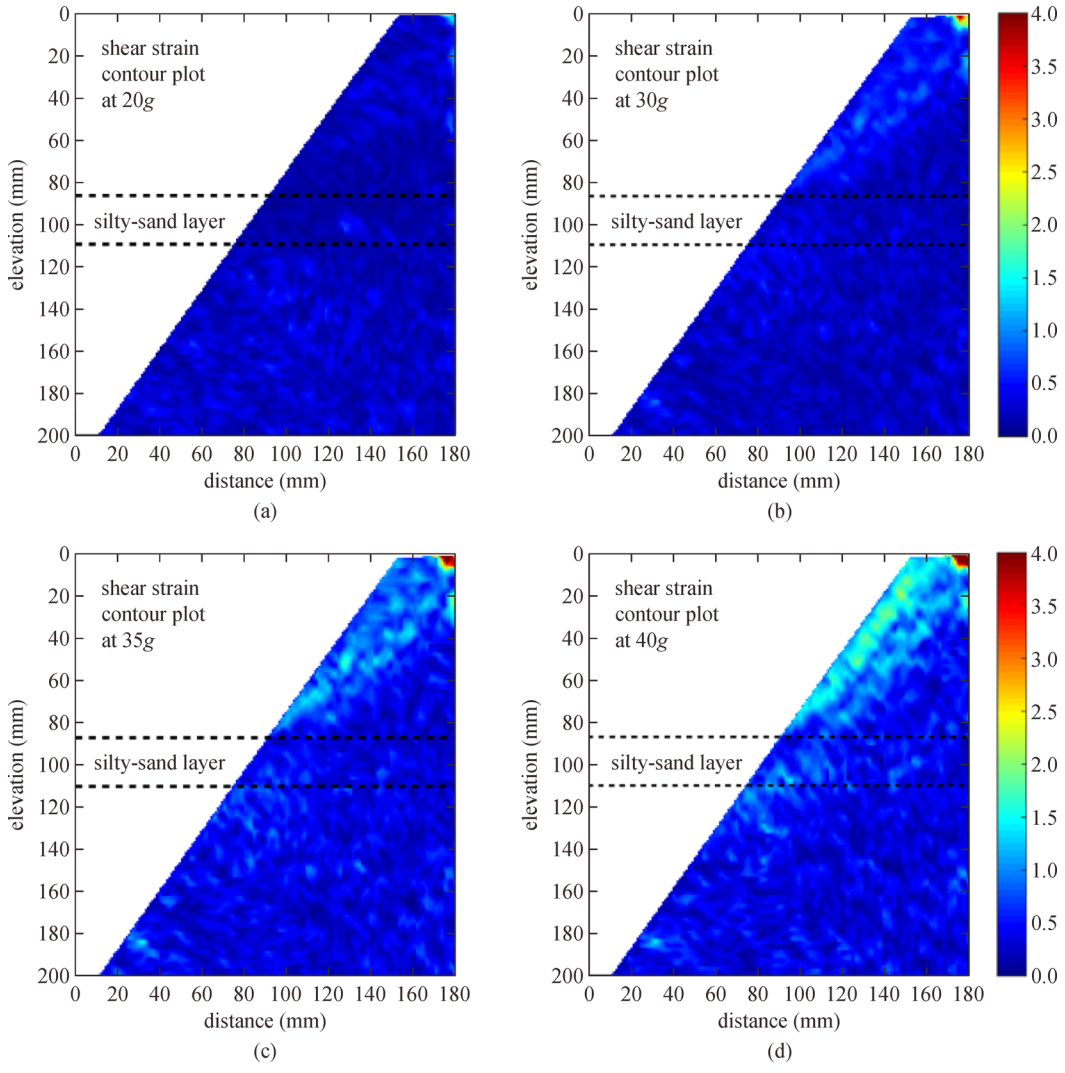


**Fig. 13** Formation of shear strain fields in non-homogeneous slope with one silty sand layer at mid-slope height during (a) 20*g*; (b) 30*g*; (c) 35*g*; (d) 40*g*.

which are triggered by the middle non-homogeneous soil layer. The shear zone is found to develop from just above the silty sand layer. At 35*g*, a single shear band can be observed, which becomes prominent at 40*g*. By comparing the images in Figs. 13(b)–13(d), it can be observed that the shear strain rates in the shear band increase very rapidly above the stronger soil layer, compared to those at places away from the silty sand layer. Thus, it may be concluded that the shear band develops from just above the stronger layer and moves toward the crown of the slope. A critical slip surface corresponding to a minimum *FOS* of 1.09 is found from the corresponding numerical analysis (refer to Fig. 10(b)). In the numerical analysis, the slip surface developed just above the stronger layer. Thus, it is concluded that the inclusion of a stronger, relatively impervious layer in the middle of a slope leads to the formation of shear bands, which essentially leads to failure. Because the value of the *FOS* is slightly greater than one, no instability is observed or predicted. It can also be noticed that the presence of a non-homogeneous soil layer creates a discontinuous shear zone (refer to Fig. 14). Because of the presence of a stronger layer at the mid-height of the slope, two shear zones have developed, with one of them located just above the stronger layer. A second, weaker shear zone starts from 50 mm above the toe and ends at the stronger soil layer. Both discontinuous shear zones that progressed during the tests are highlighted by the dash-dot line. A possible slip surface corresponding to the minimum *FOS* observed from the numerical studies is shown in Fig. 14, and is compared with the model test outcomes. The solid line shows the critical slip surface obtained from the numerical analysis, and the dashed line represents the shear band obtained from the experimental image analysis. In both the experimental and numerical results, the slip surface initiates just above the stronger layer. It can be observed that the experimental slip surface

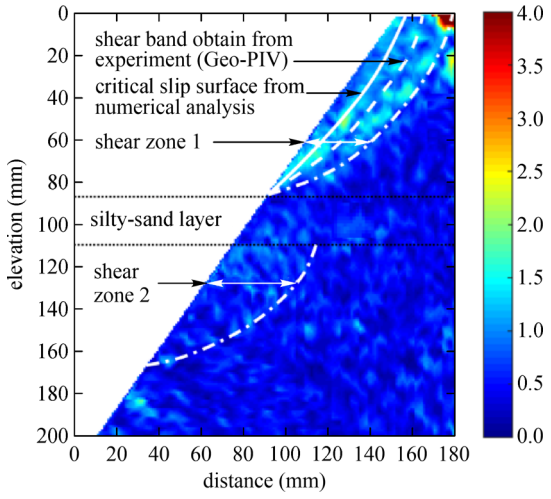


**Fig. 14** Discontinuous shear zone in non-homogeneous slope with one silty sand layer at mid-height.

grows slightly away from the numerical critical slip surfaces. The reason for this is that the obtained shear band is quite thick (see Fig. 13(d)), and the experimental slip line represents the extreme right edge of the shear band. For the case of a non-homogeneous soil layer at mid-slope height, no failure is observed in the numerical analysis. Thus, the displayed numerical slip surface shown corresponds to the calculated minimum *FOS* at 40*g*, and may not be the most critical at failure. If the experimental slip line is drawn through the right in the middle of the shear band, then both slip surfaces coincide.

Figure 15 shows the progressive nature of the shear strain fields for the case of a non-homogeneous soil slope with a stronger silty sand layer at the base of the slope. It was observed that no significant shear strains develop until 20*g*. From 30*g* onward, significant amounts of shear strains are noticeable. The shear zone is found to have developed slightly above the silty sand layer. A prominent shear band is observed from the beginning of 30*g*, which

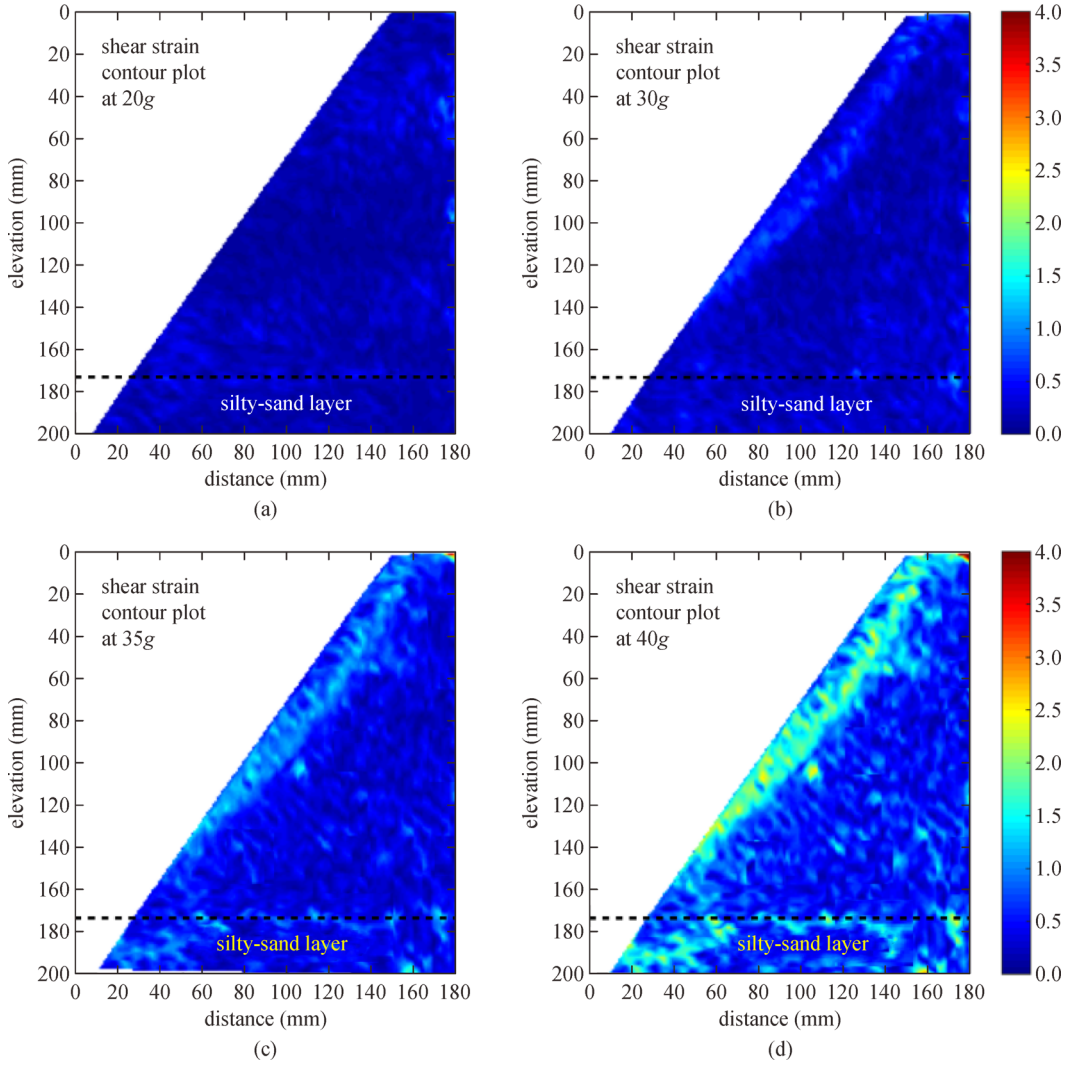


**Fig. 15** Formation of shear strain fields in non-homogeneous soil slope with a silty sand layer at the base of the slope during (a) 20*g*; (b) 30*g*; (c) 35*g*; (d) 40*g*.

becomes clearer over time. Comparing Figs. 15(b)–15(d), it is observed that the shear strain rates within the shear band increase at a higher rate, just above the stronger layer, compared with those at the other places away from the silty sand layer. Thus, it is concluded that the shear band develops from just above the stronger layer and moves toward the crown of the slope. The corresponding numerical analysis also shows a critical slip surface with an *FOS* of less than one (0.91) (refer to Fig. 10(c)). The fully developed shear band in the centrifuge tests and the critical slip surface from the corresponding numerical analysis initiates just above the stronger layer at the base of the slope. This slope was found to fail at 40*g* in the centrifuge tests. Therefore, it is concluded that the stability of an unsaturated slope is affected by the location of the less permeable stronger layer. The value of the *FOS* decreases with increasing depth of the less permeable, stronger soil layer.

## 6 Conclusions

In this study, centrifuge model tests were utilized to investigate the effects of the inclusion of a less permeable, stronger soil layer on an otherwise homogeneous, unsaturated, 55° sandy soil slope. For comparison, numerical analyses were performed for the same cases. Based on the experimental observations and the results of the numerical analyses, the following conclusions are drawn.

1) The inclusion of a relatively stronger and impermeable soil layer within otherwise homogeneous soil may trigger slope failure. It was observed that the homogeneous slope does not fail, and there was no significant shear band. On the other hand, for the case of a non-homogeneous soil slope with the same slope angle and same height, a prominent shear band was observed.

2) The presence of a less permeable, stronger soil layer at greater depth may make the slope more vulnerable. It was observed that for the case of a non-homogeneous soil slope with a stronger, less permeable silty sand layer located in the middle of the slope, failure does not occur; however, a prominent shear band was observed with an *FOS* marginally above one. On the contrary, a non-homogeneous soil slope, with a relatively impermeable, stronger silty sand layer at the base, failed to exhibit clear shear bands. In this case, the failure surface initiated just above the impermeable, stronger silty soil layer.

3) Because the relatively impermeable, stronger silty sand layer prevents the water from moving easily through it, the water content of the soil above it increases rapidly and consequently soil suction within the soil decreases. This induces a reduction in the shear strength of the soil, and a failure plane passing just above the stronger impermeable soil layer was observed.

4) The presence of a non-homogeneous, stronger, relatively impermeable soil layer creates a discontinuous shear zone. With the less permeable, stronger soil layer at the mid-height of the slope, two shear zones developed. The one just above the stronger layer was fully developed. The second one, which was partially developed, started from 50 mm above the toe and stopped at the stronger layer.

5) The study indicates that for the case of a layered soil slope, not only the shear strengths, but also the relative permeability of the layers, plays a vital role in the overall stability of the slope.

Future research should focus on the analysis of slip surface propagation under different seepage and loading conditions. The behavior of an unsaturated slope needs to be studied using analytical methods [34–36] and phase field models [37–41].

**Acknowledgements** The centrifuge tests reported here were funded by the HYDRODRIL project sponsored by the European Commission (FP7-PEOPLE-2011-IRES-Proposal No. 295225). The authors acknowledge the permissions and help received during these tests from Prof. Wei Wu, of the Institute of Geotechnical Engineering, Universität für Bodenkultur (BOKU), Vienna, Austria.

## Notation

The following symbols are used in this study:

$A$: ross-sectional area ($m^2$)

$a$: curve-fitting parameter (–)

$C'$: effective cohesion (kPa)

$C_\psi$: correction function (–)

$D_r$: relative density (%)

$g$: centrifugal acceleration ($m/s^2$)

$I$: slice index (–)

$i$: hydraulic gradient (–)

$k$: coefficient of permeability (m/s)

$k_w$: unsaturated permeability (m/s)

$k_s$: saturated permeability (m/s)

$l_{base}$: base length of each vertical slice (m)

$m$: curve-fitting parameter (–)

$N$: scaling factor (–)

$n$: curve-fitting parameter (–)

$q$: specific discharge ($m^3/s$)

$r$: distance from centrifuge axis (m)

$S$: shear strength of soil (kPa)

$\sum S_m$: total driving shear force (kPa)

$\sum S_r$: total resisting shear force (kPa)

$u_a$: pore air pressure (kPa)

$u_w$: pore water pressure (kPa)

$v$: Darcian velocity of flow (m/s)

$w$: angular velocity (m/s)

$\Theta_r$: residual volumetric water content (%)

$\Theta_s$: saturated volumetric water content (%)

$\Theta_w$: volumetric water content (%)

$\sigma_n$: total normal stress (kPa)

$\sigma_s$: suction stress (kPa)

$\phi$: effective friction angle (°)

$\phi^b$: angle defining the increase in shear strength for an increase in soil suction (°)

$\Psi$: suction pressure (kPa)

## References


1. Brown W M, Sitar N, Saarinen T F, Blair M L. Overview and summary of debris flows, landslides, and floods in the San Francisco Bay region, January 1982. In: Conference on Debris Flows, Landslides, and Floods in the San Francisco Bay region. Stanford, CA: Stanford University, 1982
2. Lagmay A M F, Ong J B T, Fernandez D F D, Lapus M R, Rodolfo R S, Tengonciang A M P, Soria J L A, Baliatan E G, Quimba Z L, Uichanco E, Paguican A. Scientists investigate recent Philippine landslide. American Geophysical Union, 2006, 87(12): 121–128
3. Dey N, Sengupta A. Effect of rainfall on the triggering of the devastating slope failure at Malin, India. Natural Hazards, 2018, 94(3): 1391–1413
4. Schuster R L, Salcedo D A, Valenzuela L. Overview of catastrophic landslides of South America in the twentieth century. Reviews in Engineering Geology, 2002, 15: 1–34
5. Van Sint Jan M, Talloni P. Sediment flow 18 June 1991 in Antofagasta: La Serena, Chile. In: The Third Chilean Congress of Geotechnical Engineering. 1993, 1: 247–265
6. Borja R, White J, Liu X, Wu W. Factor of safety in a partially saturated slope inferred from hydro-mechanical continuum modeling. International Journal for Numerical and Analytical Methods in Geomechanics, 2012, 36(2): 236–248
7. Wang D, Wang J, Wu J, Deng J, Sun M. A three-dimensional two-level gradient smoothing meshfree method for rainfall induced landslide simulations. Frontiers of Structural and Civil Engineering, 2019, 13(2): 337–352
8. Fredlund D G, Morgenstern N R, Widger R A. The shear strength of unsaturated soils. Canadian Geotechnical Journal, 1978, 15(3): 313–321
9. Lu N, Wayllace A, Oh S. Infiltration-induced seasonally reactivated instability of a highway embankment near the Eisenhower Tunnel, Colorado, USA. Engineering Geology, 2013, 162: 22–32
10. Vanapalli S K, Fredlund D G, Pufahl D E, Clifton A W. Model for the prediction of shear strength with respect to soil suction. Canadian Geotechnical Journal, 1996, 33(3): 379–392
11. Zhan L. Soil-water interaction in unsaturated expansive soil slopes. Frontiers of Structural and Civil Engineering, 2007, 1(2): 198–204
12. Wilson C J, Dietrich W E. The contribution of bedrock groundwater flow to storm runoff and high pore pressure development in hollows. IAHS-AISH Publication, 1987, 165: 49–59
13. Wu J J, Li Y, Cheng Q G, Wen H, Liang X. A simplified method for the determination of vertically loaded pile-soil interface parameters in layered soil based on FLAC 3D. Frontiers of Structural and Civil Engineering, 2016, 10(1): 103–111
14. Wu L Z, Huang R Q, Li H L, Li X, Sun P. The model tests of rainfall infiltration in two-layer unsaturated soil slopes. European Journal of Environmental and Civil Engineering, 2019, 23: 1–15
15. Chatterjee D, Murali Krishna A. Stability analysis of two-layered non-homogeneous slopes. International Journal of Geotechnical Engineering, 2018, 3: 1–7
16. Goh A T. Genetic algorithm search for critical slip surface in multiple-wedge stability analysis. Canadian Geotechnical Journal, 1999, 36(2): 382–391
17. Ho I H. Numerical study of slope-stabilizing piles in undrained clayey slopes with a weak thin layer. International Journal of Geomechanics, 2015, 15(5): 06014025
18. Al-Homoud A S, Tubeileh T K. Analysis and remedies of landslides of cut slopes due to the presence of weak cohesive layers within stronger formations. Environmental Geology, 1998, 33(4): 299–311
19. Wang R, Zhang G, Zhang J M. Centrifuge modelling of clay slope with montmorillonite weak layer under rainfall conditions. Applied Clay Science, 2010, 50(3): 386–394
20. GeoStudio. Tutorial Manual. GEO-SLOPE International Ltd, 2007
21. Dell'Avanzi E, Zornberg J G, Cabral A R. Suction profiles and scale factors for unsaturated flow under increased gravitational field. Soil and Foundation, 2004, 44(3): 79–89
22. Taylor R N. Geotechnical Centrifuge Technology. London: Taylor and Francis, 1995
23. Ng C W W, Kamchoom V, Leung A K. Centrifuge modelling of the effects of root geometry on transpiration-induced suction and stability of vegetated slopes. Landslides, 2015, 13(5): 1–14
24. Raj M, Sengupta A. Rain-triggered slope failure of the railway embankment at Malda, India. ActaGeotechnica, 2014, 9(5): 789–798
25. Zhang M, Zhang J, Lai Y. Numerical analysis for critical height of railway embankment in permafrost regions of Qinghai-Tibetan plateau. Cold Regions Science and Technology, 2005, 41(2): 111–120
26. White D J, Take W A. Geo-PIV: Particle Image Velocimetry (PIV) Software for Use in Geotechnical Testing. Technical Report. Cambridge: University of Cambridge, 2002
27. Lu N, Likos W J. Suction stress characteristic curve for unsaturated soil. Journal of Geotechnical and Geoenvironmental Engineering, 2006, 132(2): 131–142
28. Childs E C, Collis-George N. The permeability of porous materials. Proceedings of the Royal Society, 1950, 201(1066): 392–405
29. Richards L A. Capillary conduction of liquids through porous mediums. Journal of Applied Physics, 1931, 1(5): 318–333
30. van Genuchten M T. A closed-form equation for predicting the hydraulic conductivity of unsaturated soils. Soil Science Society of America Journal, 1980, 44(5): 892–898
31. Fredlund D G, Xing A. Equations for the soil-water characteristic curve. Canadian Geotechnical Journal, 1994, 31(4): 521–532
32. Bishop A W. The use of the slip circle in the stability analysis of slopes. Geotechnique, 1955, 5(1): 7–17
33. Janbu N. Application of composite slip surfaces for stability analysis. In: Proceedings of European Conference on Stability of Earth Slopes. Stockholm, 1954, 3, 43–49

34. Anitescu C, Atroshchenko E, Alajlan N, Rabczuk T. Artificial neural network methods for the solution of second order boundary value problems. Computers, Materials & Continua, 2019, 59(1): 345–359
35. Guo H, Zhuang X, Rabczuk T. A deep collocation method for the bending analysis of Kirchhoff plate. Computers, Materials & Continua, 2019, 59(2): 433–456
36. Rabczuk T, Ren H, Zhuang X. A nonlocal operator method for partial differential equations with application to electromagnetic waveguide problem. Computers, Materials & Continua, 2019, 59(1): 31–55
37. Zhou S, Zhuang X, Rabczuk T. Phase-field modeling of fluid-driven dynamic cracking in porous media. Computer Methods in Applied Mechanics and Engineering, 2019, 350: 169–198
38. Zhou S, Zhuang X, Rabczuk T. Phase field modeling of brittle compressive-shear fractures in rock-like materials: A new driving force and a hybrid formulation. Computer Methods in Applied Mechanics and Engineering, 2019, 355: 729–752
39. Zhou S, Rabczuk T, Zhuang X. Phase field modeling of quasi-static and dynamic crack propagation: COMSOL implementation and case studies. Advances in Engineering Software, 2018, 122: 31–49
40. Zhou S, Zhuang X, Rabczuk T. A phase-field modeling approach of fracture propagation in poroelastic media. Engineering Geology, 2018, 240: 189–203
41. Zhou S, Zhuang X, Zhu H, Rabczuk T. Phase field modelling of crack propagation, branching and coalescence in rocks. Theoretical and Applied Fracture Mechanics, 2018, 96: 174–192